Physical limitations on broadband scattering by heterogeneous obstacles

2007 J. Phys. A: Math. Theor. 40 11165

(http://iopscience.iop.org/1751-8121/40/36/015)

IOP Publishing Journal of Physics A: Mathematical and Theoretical

J. Phys. A: Math. Theor. **40** (2007) 11165–11182 doi:10.1088/1751-8113/40/36/015

Physical limitations on broadband scattering by heterogeneous obstacles

Christian Sohl, Mats Gustafsson and Gerhard Kristensson

Department of Electrical and Information Technology, Lund University, Sweden

Received 10 March 2007, in final form 20 July 2007
Published 21 August 2007
Online at stacks.iop.org/JPhysA/40/11165

Abstract

In this paper, new physical limitations on the extinction cross section and broadband scattering are investigated. A measure of broadband scattering in terms of the integrated extinction is derived for a large class of scatterers based on the holomorphic properties of the forward scattering dyadic. Closed-form expressions of the integrated extinction are given for the homogeneous ellipsoids, and theoretical bounds are discussed for arbitrary heterogeneous scatterers. Finally, the theoretical results are illustrated by numerical computations for a series of generic scatterers.

PACS numbers: 42.25.Fx, 42.25.Bs, 41.20.Jb

(Some figures in this article are in colour only in the electronic version)

1. Introduction

The relation between the extinction cross section and the forward scattering dyadic, nowadays known as the optical theorem, dates back to the work of Rayleigh more than a century ago [26]. Since then, the concept has fruitfully been extended to high-energy physics where it today plays an essential role in analyzing particle collisions [19]. This is one striking example of how results, with minor modifications, can be used in both electromagnetic and quantum mechanic scattering theory. Another example of such an analogy is presented in this paper, and it is believed that more analogies of this kind exist, see, e.g., the excellent books by Taylor [27] and Nussenzveig [21].

As far as the authors know, a broadband measure for scattering of electromagnetic waves was first introduced by Purcell [23] in 1969 concerning absorption and emission of radiation by interstellar dust. Purcell derived the integrated extinction for a very narrow class of scatterers via the Kramers–Kronig relations [16, pp 279–83]. A slightly different derivation of the same result was done by Bohren and Huffman [4, pp 116, 117]. In both references it was noticed that the integrated extinction is proportional to the volume of the scatterer, with proportionality factor depending only on the shape and the long wavelength limit response of the scatterer. Based upon this observation, Bohren and Huffman conjecture [4, p 117]

Figure 1. Illustration of the scattering problem. The scatterer V is subject to a plane wave incident in the $\hat{k}$-direction.

> Regardless of the shape of the particle, however, it is plausible on physical grounds that integrated extinction should be proportional to the volume of an arbitrary particle, where the proportionality factor depends on its shape and static dielectric function.

Curiosity about whether this supposition is true and the generalization of the results to a wider class of scatterers have been the main driving forces of the present study.

Physical limitations on scattering of electromagnetic waves play an important role in the understanding of wave interaction with matter. Specifically, numerous papers addressing physical limitations in antenna theory are found in the literature. Unfortunately, they are almost all restricted to the spherical geometry, deviating only slightly from the pioneering work of Chu [5] in 1948. In contrast to antenna theory, there are, however, few papers addressing physical limitations in scattering by electromagnetic waves. An invaluable exception is given by the fundamental work of Nussenzveig [20] in which both scattering by waves and particles are analyzed in terms of causality. Other exceptions of importance for the present paper are the Rayleigh scattering bounds derived by Jones [10, 11].

The results of Purcell mentioned above are generalized in several ways in this paper. The integrated extinction is proved to be valid for anisotropic heterogeneous scatterers of arbitrary shape. Specifically, this quantity is analyzed in detail for the ellipsoidal geometry. Several kinds of upper and lower bounds on broadband scattering for isotropic material models are presented. These limitations give a means of determining if an extinction cross section is realizable or not.

The paper is organized as follows: in section 2, the integrated extinction is derived for a large class of scatterers based on the holomorphic properties of the forward scattering dyadic. Next, in section 3, bounds on broadband scattering are discussed for arbitrary isotropic heterogeneous scatterers. In the following section, section 4, some closed-form expressions of the integrated extinction are given. Moreover, in section 5, numerical results on the extinction cross section are presented and compared with the theoretical bounds. Finally, some future work and possible applications are discussed in section 6.

Throughout this paper, vectors are denoted in italic bold face and dyadics in roman bold face. A hat (ˆ) on a vector denotes that the vector is of unit length.

2. Broadband scattering

The scattering problem considered in this paper is Fourier-synthesized plane wave scattering by a bounded heterogeneous obstacle of arbitrary shape, see figure 1. The scatterer is modeled by the anisotropic constitutive relations [16, chapter XI] and assumed to be surrounded by free space. The analysis presented in this paper includes the perfectly electric conducting material model, as well as general temporal dispersion with or without a conductivity term.

2.1. The forward scattering dyadic

The scattering properties of V are described by the far field amplitude, $\boldsymbol{F}$, defined in terms of the scattered field, $\boldsymbol{E}_\mathrm{s}$, as [15, section 2]

$$\boldsymbol{E}_\mathrm{s}(t,\boldsymbol{x}) = \frac{\boldsymbol{F}(\mathrm{c}_0 t - x, \hat{\boldsymbol{x}})}{x} + \mathcal{O}(x^{-2}) \qquad \text{as} \quad x \to \infty, \tag{2.1}$$

where c_0 is the speed of light in vacuum, and $\hat{\boldsymbol{x}} = \boldsymbol{x}/x$ with $x = |\boldsymbol{x}|$. The far field amplitude is related to the incident field, $\boldsymbol{E}_\mathrm{i}(\mathrm{c}_0 t - \hat{\boldsymbol{k}}\cdot\boldsymbol{x})$, which is impinging in the $\hat{\boldsymbol{k}}$-direction, via the linear and time-translational invariant convolution

$$\boldsymbol{F}(\tau,\hat{\boldsymbol{x}}) = \int_{-\infty}^{\infty} \mathbf{S}_\mathrm{t}(\tau-\tau',\hat{\boldsymbol{k}},\hat{\boldsymbol{x}})\cdot\boldsymbol{E}_\mathrm{i}(\tau')\,\mathrm{d}\tau'.$$

The dimensionless temporal scattering dyadic $\mathbf{S}_\mathrm{t}$ is assumed to be causal in the forward direction, $\hat{\boldsymbol{k}}$, in the sense that the scattered field cannot precede the incident field [20, pp 15, 16], i.e.,

$$\mathbf{S}_\mathrm{t}(\tau,\hat{\boldsymbol{k}},\hat{\boldsymbol{k}}) = \mathbf{0} \qquad \text{for} \quad \tau < 0. \tag{2.2}$$

The Fourier transform of (2.1) evaluated in the forward direction is

$$\boldsymbol{E}_\mathrm{s}(k, x\hat{\boldsymbol{k}}) = \frac{\mathrm{e}^{\mathrm{i}kx}}{x}\mathbf{S}(k,\hat{\boldsymbol{k}})\cdot\boldsymbol{E}_0 + \mathcal{O}(x^{-2}) \qquad \text{as} \quad x \to \infty,$$

where k is a complex variable in the upper half plane with $\operatorname{Re} k = \omega/\mathrm{c}_0$. Here, the amplitude of the incident field is $\boldsymbol{E}_0$, and the forward scattering dyadic, $\mathbf{S}$, is given by the Fourier representation

$$\mathbf{S}(k,\hat{\boldsymbol{k}}) = \int_{0^-}^{\infty} \mathbf{S}_\mathrm{t}(\tau,\hat{\boldsymbol{k}},\hat{\boldsymbol{k}})\,\mathrm{e}^{\mathrm{i}k\tau}\,\mathrm{d}\tau. \tag{2.3}$$

The imaginary part of k improves the convergence of (2.3) and extends the elements of $\mathbf{S}$ to holomorphic functions in the upper half plane for a large class of dyadics $\mathbf{S}_\mathrm{t}$. Recall that $\mathbf{S}(\mathrm{i}k,\hat{\boldsymbol{k}})$ is real-valued for real-valued k and $\mathbf{S}(\mathrm{i}k,\hat{\boldsymbol{k}}) = \mathbf{S}^*(-\mathrm{i}k^*,\hat{\boldsymbol{k}})$ [20, sections 1.3 and 1.4].

The scattering cross section σ_s and absorption cross section σ_a are defined as the ratio of the scattered and absorbed power, respectively, to the incident power flow density in the forward direction. The sum of the scattering and absorption cross sections is the extinction cross section,

$$\sigma_\mathrm{ext} = \sigma_\mathrm{s} + \sigma_\mathrm{a}.$$

The three cross sections are by definition real-valued and non-negative. The extinction cross section is related to the forward scattering dyadic, $\mathbf{S}$, via the optical theorem [19, pp 18–20]:

$$\sigma_\mathrm{ext}(k) = \frac{4\pi}{k}\operatorname{Im}\{\hat{\boldsymbol{p}}_\mathrm{e}^*\cdot\mathbf{S}(k,\hat{\boldsymbol{k}})\cdot\hat{\boldsymbol{p}}_\mathrm{e}\}. \tag{2.4}$$

Here, k is real-valued, and $\hat{\boldsymbol{p}}_\mathrm{e} = \boldsymbol{E}_0/|\boldsymbol{E}_0|$ is a complex-valued vector, independent of k, that represents the electric polarization, and, moreover, satisfies $\hat{\boldsymbol{p}}_\mathrm{e}\cdot\hat{\boldsymbol{k}} = 0$.

The holomorphic properties of $\mathbf{S}$ can be used to determine an integral identity for the extinction cross section. To simplify the notation, let $\varrho(k) = \hat{\boldsymbol{p}}_\mathrm{e}^*\cdot\mathbf{S}(k,\hat{\boldsymbol{k}})\cdot\hat{\boldsymbol{p}}_\mathrm{e}/k^2$. The Cauchy integral theorem with respect to the contour in figure 2 then yields

$$\varrho(\mathrm{i}\varepsilon) = \int_0^\pi \frac{\varrho(\mathrm{i}\varepsilon - \varepsilon\,\mathrm{e}^{\mathrm{i}\phi})}{2\pi}\,\mathrm{d}\phi + \int_0^\pi \frac{\varrho(\mathrm{i}\varepsilon + R\,\mathrm{e}^{\mathrm{i}\phi})}{2\pi}\,\mathrm{d}\phi + \int_{\varepsilon<|k|<R} \frac{\varrho(k+\mathrm{i}\varepsilon)}{2\pi\mathrm{i}k}\,\mathrm{d}k, \tag{2.5}$$

where k in the last integral on the right-hand side is real-valued.

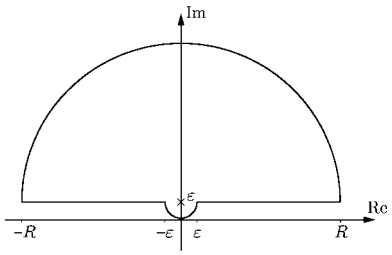

Figure 2. Integration contour used in the Cauchy integral theorem in (2.5).

The left-hand side of (2.5) and the integrand in the first integral on the right-hand side are well defined in the limit $\varepsilon \to 0$ and given by the long wavelength limit [15, p 18]:

$$\varrho(\mathrm{i}\varepsilon) = \frac{1}{4\pi}(\hat{\boldsymbol{p}}_{\mathrm{e}}^{*} \cdot \gamma_{\mathrm{e}} \cdot \hat{\boldsymbol{p}}_{\mathrm{e}} + \hat{\boldsymbol{p}}_{\mathrm{m}}^{*} \cdot \gamma_{\mathrm{m}} \cdot \hat{\boldsymbol{p}}_{\mathrm{m}}) + \mathcal{O}(\varepsilon) \qquad \text{as} \quad \varepsilon \to 0. \tag{2.6}$$

Here, $\hat{\boldsymbol{p}}_{\mathrm{m}} = \hat{\boldsymbol{k}} \times \hat{\boldsymbol{p}}_{\mathrm{e}}$ denotes the magnetic polarization and γ_{e} and γ_{m} are the electric and magnetic polarizability dyadics, respectively, see the appendix for their explicit definitions. These dyadics are real-valued and symmetric. This result also includes the effect of a conductivity term [15, pp 49–51].

The second term on the right-hand side of (2.5) is assumed to approach zero and does not contribute in the limit $R \to \infty$. This is physically reasonable since the short wavelength response of a material is non-unique from a modeling point of view [8]. The assumption is also motivated by the extinction paradox [29, pp 107–13], i.e.,

$$\varrho(k) = -\frac{A(\hat{\boldsymbol{k}})}{2\pi \mathrm{i}k}(1 + \mathcal{O}(|k|^{-1})) \qquad \text{as} \quad |k| \to \infty, \qquad \operatorname{Im} k \geqslant 0,$$

where A denotes the projected area in the forward direction.

In the last term on the right-hand side of (2.5) it is assumed that ϱ is sufficiently regular to extend the contour to the real axis. Under this assumption, the real part of (2.5) yields

$$\operatorname{Re} \varrho(0) = \frac{1}{\pi}\int_{-\infty}^{\infty} \frac{\operatorname{Im} \varrho(k)}{k}\,\mathrm{d}k = \frac{1}{4\pi^2}\int_{-\infty}^{\infty} \frac{\sigma_{\mathrm{ext}}(k)}{k^2}\,\mathrm{d}k = \frac{1}{4\pi^3}\int_{0}^{\infty} \sigma_{\mathrm{ext}}(\lambda)\,\mathrm{d}\lambda, \tag{2.7}$$

where we have used the optical theorem, (2.4). In this expression $\lambda = 2\pi/k$ is the vacuum wavelength.

In fact, the assumptions on ϱ can be relaxed, and the analysis can be generalized to certain classes of distributions [20, pp 33–43]. However, the integral in (2.7) is classically well defined for the examples considered in this paper. The relation (2.7) can also be derived using the Hilbert transform [28, chapter V].

2.2. The integrated extinction

We are now ready to utilize the main result in the previous section. Moreover, the properties of the polarizability dyadics are exploited, and the important results of Jones [10, 11] are invoked.

Insertion of the long wavelength limit (2.6) into (2.7) yields the integrated extinction

$$\int_{0}^{\infty} \sigma_{\mathrm{ext}}(\lambda)\,\mathrm{d}\lambda = \pi^2(\hat{\boldsymbol{p}}_{\mathrm{e}}^{*} \cdot \gamma_{\mathrm{e}} \cdot \hat{\boldsymbol{p}}_{\mathrm{e}} + \hat{\boldsymbol{p}}_{\mathrm{m}}^{*} \cdot \gamma_{\mathrm{m}} \cdot \hat{\boldsymbol{p}}_{\mathrm{m}}). \tag{2.8}$$

Note that (2.8) is independent of any temporal dispersion, depending only on the long wavelength limit response of the scatterer in terms of γ_{e} and γ_{m}. Closed-form expressions of γ_{e} and γ_{m} exist for the homogeneous ellipsoids, see section 4. The polarizability dyadics for more general obstacles are summarized in Kleinman and Senior [15, p 31].

For pure electric ($\gamma_m = \mathbf{0}$) and pure magnetic ($\gamma_e = \mathbf{0}$) scatterers, the integrated extinction depends only on $\hat{\boldsymbol{p}}_e$ and $\hat{\boldsymbol{p}}_m$, respectively, and hence not on $\hat{\boldsymbol{k}} = \hat{\boldsymbol{p}}_e \times \hat{\boldsymbol{p}}_m$. Moreover, the integrated extinction for a scatterer with isotropic polarizability dyadics, i.e., $\gamma_e = \gamma_e \mathbf{I}$ and $\gamma_m = \gamma_m \mathbf{I}$, is independent of $\hat{\boldsymbol{p}}_e$ and $\hat{\boldsymbol{p}}_m$ as well as $\hat{\boldsymbol{k}}$.

An important variational result can be established for isotropic material parameters with the long wavelength limit response given by the electric and magnetic susceptibilities, $\chi_e(\boldsymbol{x})$ and $\chi_m(\boldsymbol{x})$, respectively. The result states that the integrated extinction increases monotonically with increasing $\chi_e(\boldsymbol{x})$ and $\chi_m(\boldsymbol{x})$ for each $\boldsymbol{x} \in \mathbb{R}^3$ [11, theorem 1], i.e.,

$$\chi_{i1}(\boldsymbol{x}) \leqslant \chi_{i2}(\boldsymbol{x}), \qquad \boldsymbol{x} \in \mathbb{R}^3 \quad \Longrightarrow \quad \int_0^\infty \sigma_{\text{ext}1}(\lambda)\,\mathrm{d}\lambda \leqslant \int_0^\infty \sigma_{\text{ext}2}(\lambda)\,\mathrm{d}\lambda, \tag{2.9}$$

where $i = \text{e}, \text{m}$. Recall that Kramers–Kronig relations [16, pp 279–81] imply that $\chi_e(\boldsymbol{x})$ and $\chi_m(\boldsymbol{x})$ pointwise are non-negative, provided the conductivity is zero. If the conductivity of the scatterer is non-zero, the electric polarizability dyadic, γ_e, can be determined by letting the electric susceptibility becoming infinitely large [15, pp 49, 50]. As a consequence of (2.9), no heterogeneous scatterer has a larger integrated extinction than the corresponding homogeneous one with maximal susceptibility.

An important model in many applications is the perfectly conducting case (PEC), which is formally obtained—in the long wavelength limit—by the limits [15, pp 39, 40]

$$\chi_e(\boldsymbol{x}) \to \infty \qquad \text{and} \qquad \chi_m(\boldsymbol{x}) \searrow -1. \tag{2.10}$$

Since the long wavelength limit lacks a natural length scale it follows that the integrated extinction for any heterogeneous scatterer is proportional to the volume $|V| = \int_V \mathrm{dV}_{\boldsymbol{x}}$, where $\mathrm{dV}_{\boldsymbol{x}}$ is the volume measure with respect to $\boldsymbol{x}$—a result conjectured by Bohren and Huffman [4, p 117] for spherical scatterers. A brief derivation of this statement for heterogeneous, anisotropic material parameters is presented in the appendix.

Randomly oriented scatterers are valuable in many applications [23]. The broadband scattering properties of an ensemble of randomly oriented scatterers are quantified by the averaged integrated extinction,

$$\int_0^\infty \bar{\sigma}_{\text{ext}}(\lambda)\,\mathrm{d}\lambda = \frac{\pi^2}{3}\,\mathrm{tr}(\gamma_e + \gamma_m). \tag{2.11}$$

An interesting variational result based on (2.11) states that among all isotropic, homogeneous scatterers of equal volume and susceptibilities, the spherical scatterer minimizes the averaged integrated extinction [10, theorem 3].

3. Bounds on broadband scattering

The main result of section 2.2, (2.8), is now exploited. Firstly, upper and lower bounds on the integrated extinction utilizing the eigenvalue properties of the polarizability dyadics are established. These estimates are followed by two additional upper and lower bounds based on the results of Jones [10, 11].

3.1. Eigenvalue estimates

Since the extinction cross section is non-negative, it is clear that for any wavelength interval $\Lambda \subset [0, \infty)$

$$|\Lambda| \min_{\lambda \in \Lambda} \sigma(\lambda) \leqslant \int_\Lambda \sigma(\lambda)\,\mathrm{d}\lambda \leqslant \int_0^\infty \sigma_{\text{ext}}(\lambda)\,\mathrm{d}\lambda, \tag{3.1}$$

where $|\Lambda|$ is the absolute bandwidth and σ denotes any of the extinction, scattering and absorption cross sections σ_{ext}, σ_{s} and σ_{a}, respectively.

The static polarizability dyadics $\boldsymbol{\gamma}_{\mathrm{e}}$ and $\boldsymbol{\gamma}_{\mathrm{m}}$ are real-valued and symmetric, and hence diagonalizable with real-valued eigenvalues $\gamma_{\mathrm{e}j}$ and $\gamma_{\mathrm{m}j}$ with $j = 1, 2, 3$, respectively, ordered as $\gamma_{\mathrm{e}1} \geqslant \gamma_{\mathrm{e}2} \geqslant \gamma_{\mathrm{e}3}$ and $\gamma_{\mathrm{m}1} \geqslant \gamma_{\mathrm{m}2} \geqslant \gamma_{\mathrm{m}3}$. Since the right-hand side of (2.8) is the Rayleigh quotients of $\boldsymbol{\gamma}_{\mathrm{e}}$ and $\boldsymbol{\gamma}_{\mathrm{m}}$, their largest and smallest eigenvalues bound (2.8) according to standard matrix theory[1], namely,

$$\pi^2(\gamma_{\mathrm{e}3} + \gamma_{\mathrm{m}3}) \leqslant \int_0^\infty \sigma_{\mathrm{ext}}(\lambda)\,\mathrm{d}\lambda \leqslant \pi^2(\gamma_{\mathrm{e}1} + \gamma_{\mathrm{m}1}). \tag{3.2}$$

Equality on the left (right) hand side of (3.2) holds when $\hat{\boldsymbol{p}}_{\mathrm{e}}$ is a unit eigenvector of $\boldsymbol{\gamma}_{\mathrm{e}}$ with eigenvalue $\gamma_{\mathrm{e}3}$ ($\gamma_{\mathrm{e}1}$) and $\hat{\boldsymbol{p}}_{\mathrm{m}}$ simultaneously is a unit eigenvector of $\boldsymbol{\gamma}_{\mathrm{m}}$ with eigenvalue $\gamma_{\mathrm{m}3}$ ($\gamma_{\mathrm{m}1}$).

3.2. Scatterers of arbitrary shape

Broadband scattering in the sense of the integrated extinction is according to (3.2) directly related to the eigenvalues of the static polarizability dyadics. Lemma 2 in Jones [11] applied to (3.2) yields

$$\pi^2 \int_V \frac{\chi_{\mathrm{e}}(\boldsymbol{x})}{\chi_{\mathrm{e}}(\boldsymbol{x}) + 1} + \frac{\chi_{\mathrm{m}}(\boldsymbol{x})}{\chi_{\mathrm{m}}(\boldsymbol{x}) + 1}\,\mathrm{dV}_{\boldsymbol{x}} \leqslant \int_0^\infty \sigma_{\mathrm{ext}}(\lambda)\,\mathrm{d}\lambda \leqslant \pi^2 \int_V \chi_{\mathrm{e}}(\boldsymbol{x}) + \chi_{\mathrm{m}}(\boldsymbol{x})\,\mathrm{dV}_{\boldsymbol{x}}. \tag{3.3}$$

The bounds in (3.3) are sharp in the sense that equality can be obtained as a limiting process for certain homogeneous ellipsoids, see section 4.

The right-hand side of (3.3) is bounded from above by $|V|\|\chi_{\mathrm{e}} + \chi_{\mathrm{m}}\|_\infty$, where $\|f\|_\infty = \sup_{\boldsymbol{x}\in V} |f(\boldsymbol{x})|$ denotes the supremum norm. As a consequence, the upper bound on the integrated extinction for any heterogeneous scatterer is less than or equal to the integrated extinction for the corresponding homogeneous scatterer with susceptibilities $\|\chi_{\mathrm{e}}\|_\infty$ and $\|\chi_{\mathrm{m}}\|_\infty$. This observation leads to the conclusion that there is no fundamental difference on the integrated extinction between scattering by heterogeneous and homogeneous obstacles.

For weak scatterers in the sense of the Born approximation, $\|\chi_{\mathrm{e}} + \chi_{\mathrm{m}}\|_\infty \ll 1$, and (3.3) implies

$$\int_0^\infty \sigma_{\mathrm{ext}}(\lambda)\,\mathrm{d}\lambda = \pi^2 \int_V \chi_{\mathrm{e}}(\boldsymbol{x}) + \chi_{\mathrm{m}}(\boldsymbol{x})\,\mathrm{dV}_{\boldsymbol{x}} + \mathcal{O}\big(\|\chi_{\mathrm{e}} + \chi_{\mathrm{m}}\|_\infty^2\big), \tag{3.4}$$

where the Taylor series expansion $1/(1+x) = 1 + \mathcal{O}(x)$ for $|x| < 1$ has been used. Note that (3.4) reduces to a particularly simple form for homogeneous scatterers.

3.3. Star-shaped scatterers

Due to (2.9), it is possible to derive upper bounds on the integrated extinction by applying the bounds to the corresponding homogeneous scatterer with susceptibilities $\|\chi_{\mathrm{e}}\|_\infty$ and $\|\chi_{\mathrm{m}}\|_\infty$. To this end, assume V is star-shaped in the sense that $K_V \neq \emptyset$, where K_V is the set of $\boldsymbol{x} \in V$ such that for all $\boldsymbol{y} \in V$ and $0 \leqslant s \leqslant 1$ the straight line $\boldsymbol{x} + (1-s)\boldsymbol{y}$ is contained in V, i.e., if it has an interior point from which its entire boundary can be seen. For a convex scatterer, $K_V = V$.

[1] If the eigenvectors corresponding to the largest eigenvalues are the same for the electric and magnetic cases, the bounds in (3.2) can be sharpened.

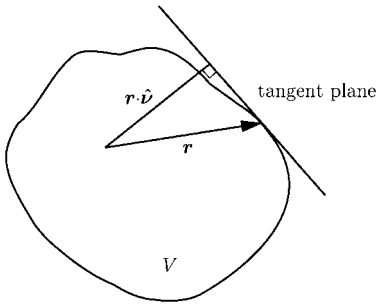

Figure 3. Geometry for the star-shape parameterization.

A refined upper bound on γ_{e1} and γ_{m1} [10, theorem 5] applied to (3.2), also taking into account the shape of V, yields the inequality

$$\int_0^\infty \sigma_{ext}(\lambda)\,d\lambda \leqslant \pi^2|V|\psi\left(\frac{\|\chi_e\|_\infty}{\psi+\|\chi_e\|_\infty}+\frac{\|\chi_m\|_\infty}{\psi+\|\chi_m\|_\infty}\right), \tag{3.5}$$

where the geometrical factor ψ is defined by

$$\psi=\frac{3}{|V|}\max_j\int_S\frac{(\hat{e}_j\cdot r)^2}{r\cdot\hat{\nu}}\,dS_r\leqslant\frac{9}{|V|}\int_S\frac{r^2}{r\cdot\hat{\nu}}\,dS_r. \tag{3.6}$$

Here, $\hat{e}_j$ denote mutually orthonormal vectors and dS_r is the surface measure of S with respect to r (S is the bounding surface of V). The denominator in (3.6) is the distance from the tangent plane to the origin, see figure 3. The upper bound in (3.6) is independent of the coordinate system orientation but depends on the location of the origin.

Furthermore, the right-hand side of (3.5) is bounded from above by either $\|\chi_e\|_\infty$ and $\|\chi_m\|_\infty$ or ψ. The first case yields (3.3) for a homogeneous scatterer (material parameters $\|\chi_e\|_\infty$ and $\|\chi_m\|_\infty$), while the latter implies

$$\int_0^\infty \sigma_{ext}(\lambda)\,d\lambda \leqslant 2\pi^2|V|\psi, \tag{3.7}$$

irrespectively of the material parameters of V. By comparing (3.3) with (3.7), it is clear that (3.7) provides the sharpest bound when $2\psi < \|\chi_e+\chi_m\|_\infty$. Note that (2.9) implies that it is possible to evaluate (3.6) for any surface circumscribing the scatterer V.

The geometrical factor for the oblate spheroid is $\psi = 3(4+\xi^{-2})/5$ and for the prolate spheroid $\psi = 3(3+2\xi^{-2})/5$ (the origin at the center of the spheroid), where $\xi \in [0,1]$ is the ratio of the minor to the major semi-axis. In particular, $\psi = 3$ for the sphere. The bound in (3.5) is isoperimetric since equality holds for the homogeneous sphere, see section 4. The geometrical factor ψ for the circular cylinder of radius b and length ℓ is[2] $\psi = \max\{3+3b^2/\ell^2, 3+\ell^2/2b^2\}$.

3.4. Jung's theorem

Jung's theorem [13] gives an optimal upper bound on the radius of a bounded subset $V \subset \mathbb{R}^3$ in terms of its diameter, diam V. The theorem states that V is contained in the unique sphere of radius $R_V \leqslant \sqrt{6}/4\,\text{diam}\,V$, with equality if and only if the closure of V contains the vertices

[2] This expression deviates from the result of Jones [10].

of a tetrahedron of edge lengths equal to diam V. Since $\psi = 3$ for the sphere and $|V|$ is bounded from above by the volume of the sphere of radius R_V, (3.5) yields

$$\int_0^\infty \sigma_{\text{ext}}(\lambda)\,\mathrm{d}\lambda \leqslant \frac{\pi^3 3\sqrt{6}}{8}(\text{diam}\,V)^3\left(\frac{\|\chi_\text{e}\|_\infty}{3+\|\chi_\text{e}\|_\infty}+\frac{\|\chi_\text{m}\|_\infty}{3+\|\chi_\text{m}\|_\infty}\right). \tag{3.8}$$

The right-hand side of (3.8) can be estimated from above independently of the material parameters. We get

$$\int_0^\infty \sigma_{\text{ext}}(\lambda)\,\mathrm{d}\lambda \leqslant \frac{\pi^3 3\sqrt{6}}{4}(\text{diam}\,V)^3,$$

which is useful in cases where the right-hand side of (3.7) diverges.

In this section, we have applied Jung's theorem to a sphere circumscribing the scatterer. There are, however, other choices of circumscribing surfaces that can be utilized [9].

4. Homogeneous ellipsoidal scatterers

For homogeneous, anisotropic ellipsoidal scatterers with susceptibility dyadics $\boldsymbol{\chi}_\text{e}$ and $\boldsymbol{\chi}_\text{m}$, closed-form expressions of $\boldsymbol{\gamma}_\text{e}$ and $\boldsymbol{\gamma}_\text{m}$ exist [12], namely,

$$\boldsymbol{\gamma}_i = |V|\boldsymbol{\chi}_i \cdot (\mathbf{I}+\mathbf{L}\cdot\boldsymbol{\chi}_i)^{-1}, \qquad i = \text{e},\text{m} \tag{4.1}$$

where $\mathbf{L}$ and $\mathbf{I}$ are the depolarizing and unit dyadics in $\mathbb{R}^3$, respectively. In terms of the semi-axes a_j in the $\hat{\boldsymbol{e}}_j$-direction, the volume $|V| = 4\pi a_1 a_2 a_3/3$. The depolarizing dyadic has unit trace, and is real-valued and symmetric [30], and, hence, diagonalizable with real-valued eigenvalues. Its eigenvalues are the depolarizing factors L_j [6, 22]:

$$L_j = \frac{a_1 a_2 a_3}{2}\int_0^\infty \frac{\mathrm{d}s}{(s+a_j^2)\sqrt{(s+a_1^2)(s+a_2^2)(s+a_3^2)}}, \qquad j = 1,2,3. \tag{4.2}$$

The depolarizing factors satisfy $0 \leqslant L_j \leqslant 1$ and $\sum_j L_j = 1$.

Closed-form expressions of (4.2) exist in the special case of the ellipsoids of revolution, i.e., the prolate and oblate spheroids. In terms of the eccentricity $e = \sqrt{1-\xi^2}$, where $\xi \in [0,1]$ is the ratio of the minor to the major semi-axis, the depolarizing factors are (symmetry axis along the $\hat{\boldsymbol{e}}_3$-direction)

$$L_1 = L_2 = \frac{1}{4e^3}\left(2e-(1-e^2)\ln\frac{1+e}{1-e}\right), \qquad L_3 = \frac{1-e^2}{2e^3}\left(\ln\frac{1+e}{1-e}-2e\right), \tag{4.3}$$

and

$$L_1 = L_2 = \frac{1-e^2}{2e^2}\left(-1+\frac{\arcsin e}{e\sqrt{1-e^2}}\right), \qquad L_3 = \frac{1}{e^2}\left(1-\frac{\sqrt{1-e^2}}{e}\arcsin e\right),$$

for the prolate and oblate spheroids, respectively. In particular, $L_j = 1/3$ for the sphere.

The integrated extinction for anisotropic homogeneous ellipsoidal scatterers is given by (4.1) inserted into (2.8). The result is

$$\int_0^\infty \sigma_{\text{ext}}(\lambda)\,\mathrm{d}\lambda = \pi^2|V|\sum_{i=\text{e},\text{m}} \hat{\boldsymbol{p}}_i^* \cdot \boldsymbol{\chi}_i \cdot (\mathbf{I}+\mathbf{L}\cdot\boldsymbol{\chi}_i)^{-1}\cdot\hat{\boldsymbol{p}}_i. \tag{4.4}$$

For isotropic material parameters, $\boldsymbol{\chi}_\text{e} = \chi_\text{e}\mathbf{I}$ and $\boldsymbol{\chi}_\text{m} = \chi_\text{m}\mathbf{I}$, (4.4) reduces to

$$\int_0^\infty \sigma_{\text{ext}}(\lambda)\,\mathrm{d}\lambda = \pi^2|V|\sum_{j=1}^3\left(\frac{\kappa_{\text{e}j}\chi_\text{e}}{1+\chi_\text{e}L_j}+\frac{\kappa_{\text{m}j}\chi_\text{m}}{1+\chi_\text{m}L_j}\right), \tag{4.5}$$

where $\kappa_{\mathrm{e}j} = |\hat{\boldsymbol{p}}_{\mathrm{e}} \cdot \hat{\boldsymbol{e}}_j|^2$ and $\kappa_{\mathrm{m}j} = |\hat{\boldsymbol{p}}_{\mathrm{m}} \cdot \hat{\boldsymbol{e}}_j|^2$ are the polarization vectors projected onto the mutually orthonormal vectors $\hat{\boldsymbol{e}}_j$. Note that $\sum_j \kappa_{\mathrm{e}j} = \sum_j \kappa_{\mathrm{m}j} = 1$ and that the averaged integrated extinction is characterized by $\kappa_{\mathrm{e}j} = \kappa_{\mathrm{m}j} = 1/3$. For prolate and oblate spheroids, which are axially symmetric with respect to the $\hat{\boldsymbol{e}}_3$-axis, a plane wave incident at an angle θ to this axis yields

$$\begin{cases} \kappa_{\mathrm{e}1} + \kappa_{\mathrm{e}2} = 1 \\ \kappa_{\mathrm{e}3} = 0 \\ \kappa_{\mathrm{m}1} + \kappa_{\mathrm{m}2} = \cos^2\theta \\ \kappa_{\mathrm{m}3} = \sin^2\theta \end{cases} \quad \text{(TE)} \qquad \begin{cases} \kappa_{\mathrm{m}1} + \kappa_{\mathrm{m}2} = 1 \\ \kappa_{\mathrm{m}3} = 0 \\ \kappa_{\mathrm{e}1} + \kappa_{\mathrm{e}2} = \cos^2\theta \\ \kappa_{\mathrm{e}3} = \sin^2\theta \end{cases} \quad \text{(TM)}.$$

In the limit as the volume goes to zero, the integrated extinction vanishes for a scatterer with finite susceptibilities. To obtain a non-zero integrated extinction, either the scatterer has to be conducting or evaluated in the high-contrast limit see, e.g., the PEC disc below. In the long wavelength PEC limit, see (2.10), the integrated extinction becomes

$$\int_0^\infty \sigma_{\mathrm{ext}}(\lambda)\,\mathrm{d}\lambda = \pi^2|V| \sum_{j=1}^{3} \left(\frac{\kappa_{\mathrm{e}j}}{L_j} - \frac{\kappa_{\mathrm{m}j}}{1 - L_j} \right). \tag{4.6}$$

The right-hand side of (4.5) is bounded from above by χ_i and from below by $\chi_i/(1+\chi_i)$. The bounds in (3.3) are sharp in the sense that χ_i and $\chi_i/(1+\chi_i)$ are obtained at arbitrary precision for the infinite needle and disc of constant volume $|V|$, respectively. In fact, the upper bound holds for an infinite needle oriented along the $\hat{\boldsymbol{e}}_3$-direction ($L_1 + L_2 = 1$) with parallel polarization ($\kappa_{i3} = 1$). The corresponding equality for the lower bound holds for the infinite disc with unit normal vector $\hat{\boldsymbol{e}}_3$ ($L_3 = 1$) and parallel polarization ($\kappa_{i3} = 1$).

A simple example of (4.5) is given by the homogeneous sphere for which the integrated extinction is equal to $3\pi^2|V|\sum_i \chi_i/(\chi_i + 3)$ independent of $\kappa_{\mathrm{e}j}$ and $\kappa_{\mathrm{m}j}$, which also is the result of Bohren and Huffman for the non-magnetic case [4, p 117]. In particular, the PEC limit (2.10) implies that the integrated extinction for the sphere is equal to $3\pi^2|V|/2$. Similar results for stratified dielectric spheres are obtained using recursive compositions of Möbius transformations. For the case of two layers, see section 5.4.

The integrated extinction for the PEC elliptic disc is given by (4.6), and the integrals in (4.2), as the semi-axis a_3 approaches zero, are available in the literature [6, p 507], [22]. The result is

$$\begin{cases} L_1/|V| = \dfrac{3}{4\pi a^3 e^2}(K - E) \\ L_2/|V| = \dfrac{3}{4\pi a^3 e^2}(E/(1-e^2) - K) \\ (L_3 - 1)/|V| = -\dfrac{3E}{4\pi a^3(1-e^2)} \end{cases}$$

where a is the major semi-axis, and $E = E(e^2)$ and $K = K(e^2)$ are the complete elliptic integrals of first and second kinds, respectively [1, p 590]. We obtain

$$\int_0^\infty \sigma_{\mathrm{ext}}(\lambda)\,\mathrm{d}\lambda = \frac{4\pi^3 a^3}{3} \begin{cases} B\cos^2\phi + C\sin^2\phi - A\sin^2\theta & \text{(TE)} \\ (B\sin^2\phi + C\cos^2\phi)\cos^2\theta & \text{(TM)} \end{cases} \tag{4.7}$$

where θ and ϕ are the spherical angles of the incident direction, $\hat{\boldsymbol{k}}$. The factors A, B and C are defined as

$$A = \frac{1-e^2}{E}, \qquad B = \frac{e^2(1-e^2)}{E - (1-e^2)K}, \qquad C = \frac{e^2}{K - E}.$$

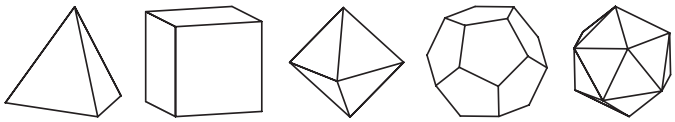

Figure 4. The integrated extinctions for the Platonic solids based on MoM calculations [24]. The Platonic solids are from left to right the tetrahedron, hexahedron, octahedron, dodecahedron and icosahedron, with 4, 6, 8, 12 and 20 faces, respectively.

Table 1. The eigenvalues γ_e and the integrated extinction for the Platonic solids in units of $|V|$ in the high-contrast limit $\chi_e \to \infty$. The last column gives the volume of the Platonic solids expressed in the edge length a.

Platonic solids	$\gamma_e/\|V\|$	γ_e/a^3	Integrated extinctions	$\|V\|/a^3$
Tetrahedron	5.03	0.593	$49.6\|V\|$	$\sqrt{2}/12$
Hexahedron	3.64	3.64	$35.9\|V\|$	1
Octahedron	3.55	1.67	$35.0\|V\|$	$\sqrt{2}/3$
Dodecahedron	3.18	24.4	$31.4\|V\|$	$(15+7\sqrt{5})/4$
Icosahedron	3.13	6.83	$30.9\|V\|$	$5(3+\sqrt{5})/12$

Note that the TM polarization vanishes for $\theta = \pi/2$ independently of $\phi \in [0, 2\pi)$. The integrated extinction (4.7) can also be derived from the long wavelength limit of the T-matrix approach [3].

5. Numerical results

In this section, we illustrate the theoretical results obtained above by several numerical examples. Specifically, we calculate the extinction cross sections and the eigenvalues of the polarizability dyadics for a set of scatterers with isotropic material parameters. These results are then compared to the theoretical results presented in sections 2–4. The effect of temporal dispersion is exemplified with the Lorentz dispersive cylinder and the Debye dispersive non-spherical raindrop in sections 5.2 and 5.3, respectively. In section 5.4, a stratified sphere is considered to illustrate the effect of heterogeneous and magnetic material properties. A parameter study of the PEC needle illustrates an object with negligible polarizability dyadics in the limit of vanishing semi-axis ratio in section 5.5.

5.1. Platonic solids

Since the homogeneous Platonic solids are invariant under a set of appropriate point groups, their polarizability dyadics are isotropic. By (2.8) this implies that the integrated extinctions are independent of both polarization and incident directions. The five Platonic solids are depicted in figure 4, see also table 1, together with the integrated extinctions in the non-magnetic, high-contrast limit, i.e., $\chi_e \to \infty$.

A common lower bound on the integrated extinctions in figure 4 is obtained by (4.5) for the volume-equivalent sphere. This lower bound is motivated by Jones' result [10, theorem 3] and the fact that the polarizability dyadics are isotropic. The result is $14.80|V|$.

Upper bounds on the integrated extinctions are given by the smallest circumscribing high-contrast spheres, which based on solid geometry are found to be $241.60|V|$, $80.54|V|$, $61.98|V|$, $44.62|V|$ and $48.96|V|$ for the tetrahedron, hexahedron,

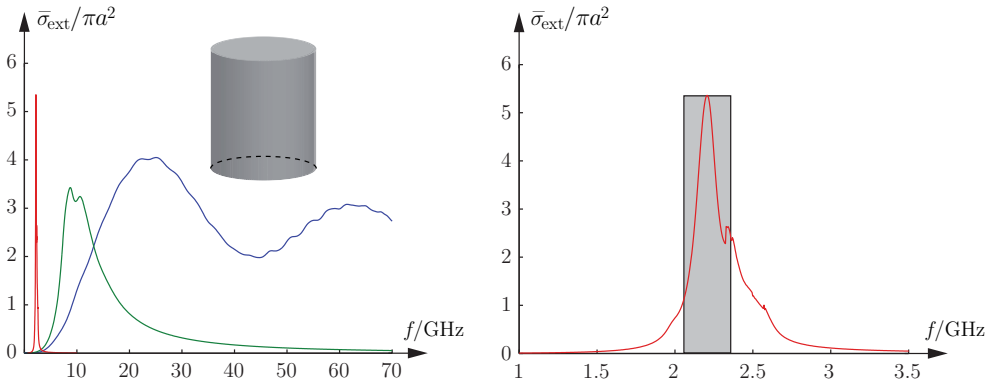

Figure 5. The averaged extinction cross section, $\bar{\sigma}_{\text{ext}}$, in units of πa^2 as a function of the frequency in GHz for a non-magnetic Lorentz dispersive circular cylinder with volume-equivalent sphere of radius $a = 1$ cm. The three curves in the left figure have the same long wavelength response $\chi_{\text{e}} = 1$. The first two curves with peaks at 2 GHz and 10 GHz are Lorentz dispersive, while the third curve is non-dispersive. The right figure is a close-up of the 2 GHz peak in the left figure.

octahedron, dodecahedron and icosahedron, respectively, see (2.9). The upper and lower bounds are seen to be quite close to the numerical values presented in figure 4, at least for the dodecahedron and icosahedron, which do not deviate much from the volume-equivalent sphere. Since the Platonic solids are star-shaped with respect to all interior points, a somewhat different set of upper bounds can be derived from (3.5).

5.2. Lorentz dispersive circular cylinder

The averaged extinction cross section, $\bar{\sigma}_{\text{ext}}$, as a function of the frequency for a Lorentz dispersive circular cylinder is depicted in figure 5. The ratio of the cylinder length ℓ to its radius b is $\ell/b = 2$. The cylinder is non-magnetic with electric susceptibility given by the Lorentz model [4, section 9.1]:

$$\chi_{\text{e}}(\omega) = \frac{\omega_{\text{p}}^2}{\omega_0^2 - \omega^2 - \text{i}\omega\nu},$$

where ω_{p} is the plasma frequency, ν is the collision frequency and ω_0 is the resonance frequency. Explicit values of ω_{p}, ω_0 and ν are $\omega_{\text{p}} = \omega_0 = 4\pi \cdot 10^9$ rad s^{-1}, $\nu = 0.7 \cdot 10^9$ rad s^{-1} and $\omega_{\text{p}} = \omega_0 = 20\pi \cdot 10^9$ rad s^{-1}, $\nu = 10^{10}$ rad s^{-1}, respectively. The Lorentz parameters are chosen such that all three curves in the left figure have the same long wavelength susceptibility $\chi_{\text{e}} = \chi_{\text{e}}(0) = 1$. The first two curves with peaks at 2 GHz and 10 GHz depict the dispersive case, while the third for comparison illustrates the results for the non-dispersive case. The three curves in the left figure have the same integrated extinctions, since their long wavelength susceptibilities coincide. The calculation is based on the T-matrix approach [18].

A numerical calculation of the eigenvalues of the polarizability dyadic for the dielectric cylinder is performed by adopting the finite element method (FEM). The results are $0.773|V|$, $0.749|V|$ and $0.749|V|$. This result implies that the numerically computed averaged extinction cross section, $\bar{\sigma}_{\text{ext}}$, in (2.11) is $7.47|V|$. The numerically calculated integrated extinction in the interval $f \in [0, 70]$ GHz is $7.43|V|$ for the first and $7.44|V|$ for the second curve in figure 5.

Common lower and upper bounds on the integrated extinctions based on (3.3) are $4.94|V|$ and $9.87|V|$, respectively. A sharper lower bound is $7.40|V|$ corresponding to the

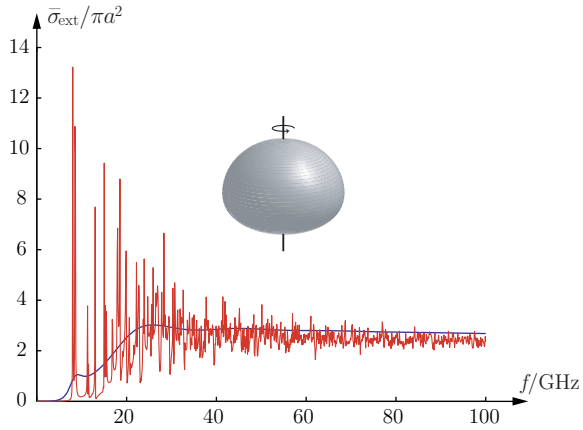

Figure 6. The averaged extinction cross section, $\bar{\sigma}_{\rm ext}$, in units of πa^2 as a function of the frequency in GHz for a raindrop of volume-equivalent radius $a = 2$ mm. The smooth curve is for the Debye model (5.1), while the oscillatory curve is for the non-dispersive case. The two curves have the same long wavelength response and therefore also the same integrated extinctions.

volume-equivalent sphere. An upper bound can for comparison be obtained from (3.5). For $\ell/b = 2$ this implies $\psi = 5$ and the upper bound $8.23|V|$, which is sharper than the bound based on (3.3).

The figure on the right-hand side of figure 5 is a close-up of the 2 GHz peak. The boundary curve of the box corresponds to an artificial scatterer with averaged extinction cross section supported at the peak, i.e., for an averaged extinction cross section that vanishes everywhere outside the box. The integrated extinction for the boundary curve of the box and the three curves in the left-hand side of figure 5 coincide.

5.3. Debye dispersive non-spherical raindrop

The averaged extinction cross section, $\bar{\sigma}_{\rm ext}$, as a function of the frequency for a falling raindrop in figure 6. The axially symmetric drop depicted in figure 6 is parameterized by the polar angle θ and the radial distance

$$r(\theta) = r_0 \left(1 + \sum_{k=0}^{10} c_k \cos k\theta\right),$$

where r_0 is determined from the condition of the volume equivalence with the sphere of radius a, i.e., $|V| = \frac{2\pi}{3}\int_0^\pi r^3(\theta)\sin\theta\,\mathrm{d}\theta$ with $|V| = 4\pi a^3/3$. The radius of the volume-equivalent sphere used in figure 6 is $a = 2$ mm with associated shape coefficients $c_0 = -0.0458$, $c_1 = 0.0335$, $c_2 = -0.1211$, $c_3 = 0.0227$, $c_4 = 0.0083$, $c_5 = -0.0089$, $c_6 = 0.0012$, $c_7 = 0.0021$, $c_8 = -0.0013$, $c_9 = -0.0001$ and $c_{10} = 0.0008$ [2]. The calculation is based on the T-matrix approach [18].

The smooth curve in figure 6 is for the non-magnetic Debye model [4, section 9.5]

$$\chi_{\rm e}(\omega) = \chi_\infty + \frac{\chi_{\rm s} - \chi_\infty}{1 - \mathrm{i}\omega\tau}, \tag{5.1}$$

where τ is the relaxation time and χ_∞ and $\chi_{\rm s}$ are the short and long wavelength susceptibilities, respectively. Pure water at 20 °C is considered with $\chi_{\rm s} = 79.2$, $\chi_\infty = 4.6$ and $\tau = 9.36$ ps [14, p 43]. The curve with largest variation is for the non-dispersive case with a susceptibility identical to the long wavelength limit, $\chi_{\rm s}$, of (5.1).

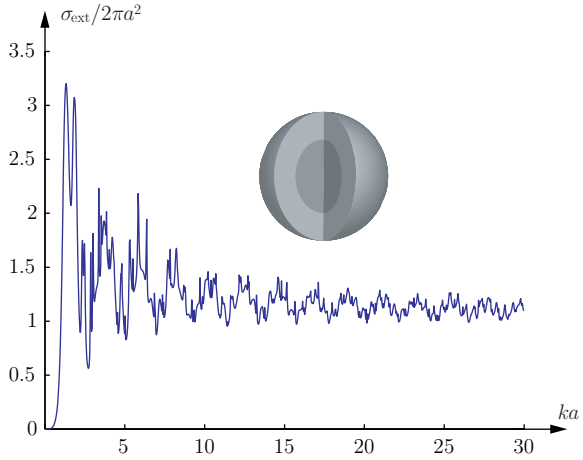

Figure 7. The extinction cross section, σ_{ext}, in units of $2\pi a^2$ as a function of the radius ka for a dielectric stratified sphere with two layers of equal volume. The electric and magnetic susceptibilities are $\chi_{\text{e}1} = 2$ and $\chi_{\text{m}1} = 1$ for the core and $\chi_{\text{e}2} = 1$ and $\chi_{\text{m}2} = 2$ for the outer layer.

Since the long wavelength susceptibilities coincide for the two curves in figure 6, their integrated extinctions are equal according to (2.11). The eigenvalues of the polarizability dyadics for the raindrop can be obtained by numerical computations. A finite element method (FEM) computation gives the three eigenvalues: $2.43|V|$, $3.21|V|$ and $3.21|V|$, respectively. This result implies that the numerically computed averaged extinction cross section, $\bar{\sigma}_{\text{ext}}$, in (2.11) is $29.1|V|$. If we numerically integrate the average extinction cross section in figure 6 over $f \in [0, 100]$ GHz, we get $26.4|V|$ for the dispersive and $25.6|V|$ for the non-dispersive curve, respectively.

Lower and upper bounds on the integrated extinctions, given by (3.3), are $9.75|V|$ and $782|V|$, respectively, which are rather crude. A more accurate lower bound is given by the non-magnetic, volume-equivalent sphere with static susceptibilities $\chi_{\text{e}} = \chi_{\text{s}}$, for which (4.5) yields $28.5|V|$. The star-shaped bound in section 3.3 is also applicable. The result for the raindrop is $32.15|V|$. We observe that both the lower and upper bounds approximate the true value very well.

5.4. Stratified sphere

Due to spherical symmetry, the polarizability dyadics of a stratified sphere are isotropic and easily computed by recursive applications of Möbius transformations. In particular, the integrated extinction for two layers with electric and magnetic susceptibilities $\chi_{\text{e}1}$ and $\chi_{\text{m}1}$ in the core, and $\chi_{\text{e}2}$ and $\chi_{\text{m}2}$ in the outer layer, respectively, is

$$\int_0^\infty \sigma_{\text{ext}}(\lambda)\,\mathrm{d}\lambda = 3\pi^2|V| \sum_{i=\text{e,m}} \frac{\chi_{i2}(\chi_{i1}+2\chi_{i2}+3)+\varsigma^3(2\chi_{i2}+3)(\chi_{i1}-\chi_{i2})}{(\chi_{i2}+3)(\chi_{i1}+2\chi_{i2}+3)+2\varsigma^3\chi_{i2}(\chi_{i1}-\chi_{i2})}, \tag{5.2}$$

where ς is the ratio of the inner to the outer radius. The special cases $\varsigma = 0$ and $\varsigma = 1$ correspond to homogeneous spheres with susceptibilities χ_{i2} and χ_{i1}, respectively, see section 4. Moreover, both $\chi_{i1} = \chi_{i2}$ and $\chi_{i2} = 0$ yield the homogeneous sphere of susceptibility χ_{i1}, with the volume of the sphere being a fraction ς^3 of the volume $|V|$ in the latter case.

The extinction cross section, σ_{ext}, as a function of the radius ka for the stratified sphere with two layers of equal volume, $\varsigma = 1/\sqrt[3]{2}$, is depicted in figure 7. The used susceptibilities

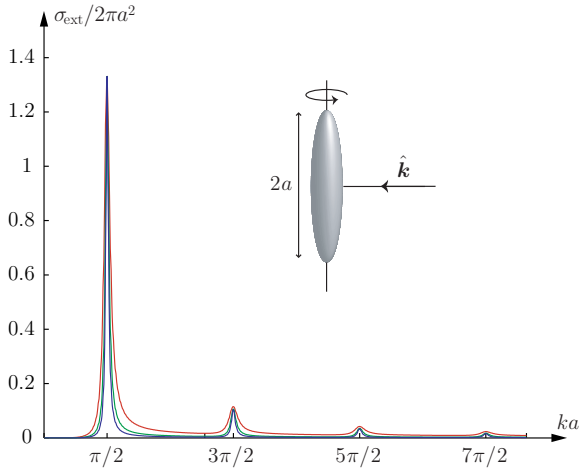

Figure 8. The extinction cross section, σ_{ext}, in units of $2\pi a^2$ as a function of ka for the PEC needle of length $2a$. The needle is approximated by a prolate spheroid with semi-axis ratio 10^{-3} for the outermost, 10^{-5} for the intervening and 10^{-7} for the innermost curve. The calculation is based on the T-matrix approach [3].

are $\chi_{\text{e1}} = 2$ and $\chi_{\text{m1}} = 1$ in the core, and $\chi_{\text{e2}} = 1$ and $\chi_{\text{m2}} = 2$ in the outer layer. The calculations are based on the Mie-series approach [17]. Note that the curve in figure 7 approaches twice the geometrical cross section area in the short wavelength limit. Compare this observation with the extinction paradox [29, pp 107, 108].

The numerically integrated extinction is $19.1|V|$ for $ka \in [0, 30]$ and $19.3|V|$ for $ka \in [0, 100]$, with relative errors of 1.7% and 0.5%, respectively, compared to the theoretical value $19.4|V|$ given by (5.2).

Lower and upper bounds on the integrated extinction based on the inequality in (2.9) are $14.8|V|$ and $23.7|V|$, respectively, corresponding to the volume-equivalent homogeneous sphere with minimal and maximal susceptibilities, $\inf_{x\in V} \chi_i$ and $\sup_{x\in V} \chi_i$, respectively. Note that this upper bound coincides with the one obtained from (3.5), but that both the lower and upper bounds based on (2.9) are sharper than those given by (3.3).

5.5. PEC needle

The integrated extinction for the PEC needle of length $2a$ oriented along the $\hat{e}_3$-direction is given by (4.3) and (4.6) in the limit $\xi \to 0$. The result is

$$\int_0^\infty \sigma_{\text{ext}}(\lambda)\,\mathrm{d}\lambda = \frac{4\pi^3 a^3}{3} \begin{cases} \mathcal{O}(\xi^2) & \text{(TE)} \\ \dfrac{\sin^2\theta}{\ln 2/\xi - 1} + \mathcal{O}(\xi^2) & \text{(TM)}. \end{cases} \tag{5.3}$$

The right-hand side of (5.3) can also be derived from the long wavelength limit of the T-matrix [3].

The integrated extinction (5.3) is seen to vanish for both polarizations in the limit $\xi \to 0$. Since the extinction cross section is non-negative, this implies that it vanishes almost everywhere except on a set of measure zero consisting of the denumerable resonances for which an integer multiple of $\lambda/2$ coincides with the length of the needle. This result is illustrated numerically in figure 8, which shows the extinction cross section, σ_{ext}, for the PEC needle for the TM polarization at normal incidence. Note that, due to symmetry, only

resonances corresponding to ka equal to an odd multiple of $\pi/2$ are excited at normal incidence. The numerically integrated extinctions in figure 8 agree well with (5.3). The relative errors are less than 0.5% with an integration interval $ka \in [0, 12]$ for the three curves.

6. Concluding remarks

The integrated extinction is an example of what is referred to in modern physics as a sum rule or a dispersion relation [20]. The mathematical derivation of the dispersion relations is based on the assumption that certain linear and causal physical quantities with known high-frequency (short wavelength) asymptotic are boundary values of holomorphic functions in the frequency variable.

The major results of this paper are the proof and illustrations of the integrated extinction for linear, passive, and anisotropic scatterers. It is shown that the integrated extinction is monotonically increasing in the material properties. Moreover, the electric and magnetic material properties contribute equally to the integrated extinction. It is also shown that the integrated extinction is useful in deriving physical limitations on broadband scattering.

The integrated extinction is particularly important from an antenna point of view, since it generalizes the physical limitations on the antenna performance derived by Chu [5] for the smallest circumscribing sphere. These new limitations, which can be shown to relate bandwidth and directivity of any antenna in terms of volume and shape, are reported in [7]. The integrated extinction is also of great interest in applications to broadband scattering by artificial material models such as metamaterials. In this application, it provides physical limitations on scattering by general material models [25]. Moreover, the bounds presented in section 3 may be of use to bound material parameters in inverse scattering problems. All these applications to material modeling and inverse scattering problems are currently under investigation and will be reported in forthcoming papers.

Additional theoretical work on the integrated extinction also includes bi-anisotropy and diamagnetics, which will be reported elsewhere. Finally, it should be noted that the concept of the integrated extinction with minor changes also holds in linear acoustics [15, section 7].

Acknowledgment

The financial support by the Swedish Research Council is gratefully acknowledged.

Appendix. The polarizability dyadics

For an anisotropic scatterer modeled by the material dyadic $\boldsymbol{\tau}$ (electric susceptibility dyadic $\boldsymbol{\chi}_{\mathrm{e}}$ without a conductivity term or magnetic susceptibility dyadic $\boldsymbol{\chi}_{\mathrm{m}}$), the total electric field $\boldsymbol{E}$ (similarly for the magnetic field $\boldsymbol{H}$) satisfies

$$\begin{cases} \nabla \times \boldsymbol{E}(\boldsymbol{x}) = \mathbf{0} \\ \nabla \cdot ((\boldsymbol{\tau}(\boldsymbol{x}) + \mathbf{I}) \cdot \boldsymbol{E}(\boldsymbol{x})) = 0 \end{cases} \qquad \boldsymbol{x} \in \mathbb{R}^3.$$

Here, $\boldsymbol{\tau}$ is assumed to be a symmetric dyadic at all points $\boldsymbol{x}$ and sufficiently regular to justify the operations below.

Decompose the total field $\boldsymbol{E}$ as $\boldsymbol{E}_j = E_0 \hat{\boldsymbol{e}}_j + \boldsymbol{E}_{\mathrm{s}j}$, where $j = 1, 2, 3$. The pertinent partial differential equation for the scattered field $\boldsymbol{E}_{\mathrm{s}j}$ is then

$$\begin{cases} \nabla \times \boldsymbol{E}_{\mathrm{s}j}(\boldsymbol{x}) = \mathbf{0} \\ \nabla \cdot ((\boldsymbol{\tau}(\boldsymbol{x}) + \mathbf{I}) \cdot \boldsymbol{E}_{\mathrm{s}j}(\boldsymbol{x})) = -E_0 \nabla \cdot (\boldsymbol{\tau}(\boldsymbol{x}) \cdot \hat{\boldsymbol{e}}_j) \end{cases} \qquad \boldsymbol{x} \in \mathbb{R}^3 \tag{A.1}$$

together with the asymptotic condition $\boldsymbol{E}_{\mathrm{s}j}(\boldsymbol{x}) \to \mathcal{O}(|\boldsymbol{x}|^{-3})$ as $|\boldsymbol{x}| \to \infty$.

The first condition in (A.1) implies that there exists a potential Φ_j related to the scattered field as $\boldsymbol{E}_{sj} = -\nabla\Phi_j$ satisfying

$$\begin{cases} \nabla\cdot((\boldsymbol{\tau}(\boldsymbol{x})+\mathbf{I})\cdot\nabla\Phi_j(\boldsymbol{x})) = E_0\nabla\cdot(\boldsymbol{\tau}(\boldsymbol{x})\cdot\hat{\boldsymbol{e}}_j) \\ \Phi_j(\boldsymbol{x}) \to \mathcal{O}(|\boldsymbol{x}|^{-2}) \qquad \text{as} \quad |\boldsymbol{x}|\to\infty \end{cases} \qquad \boldsymbol{x}\in\mathbb{R}^3. \tag{A.2}$$

This problem has a unique solution. The entries of the polarizability dyadic $\boldsymbol{\gamma}$ ($\boldsymbol{\gamma}_{\mathrm{e}}$ or $\boldsymbol{\gamma}_{\mathrm{m}}$ depending on whether the problem is electric or magnetic) are then ($i, j = 1, 2, 3$)

$$\hat{\boldsymbol{e}}_i\cdot\boldsymbol{\gamma}\cdot\hat{\boldsymbol{e}}_j = \frac{1}{E_0}\hat{\boldsymbol{e}}_i\cdot\int_{\mathbb{R}^3}\boldsymbol{\tau}(\boldsymbol{x})\cdot\boldsymbol{E}_j(\boldsymbol{x})\,\mathrm{dV}_{\boldsymbol{x}}. \tag{A.3}$$

Scale this solution by a factor α, i.e., let $\boldsymbol{x}\longrightarrow\boldsymbol{x}' = \alpha\boldsymbol{x}$, with material dyadic $\boldsymbol{\tau}'(\boldsymbol{x}') = \boldsymbol{\tau}(\boldsymbol{x})$, and denote the solution to the new problem by $\Phi'_j(\boldsymbol{x}')$. The new problem then satisfies

$$\begin{cases} \nabla'\cdot((\boldsymbol{\tau}'(\boldsymbol{x}')+\mathbf{I})\cdot\nabla'\Phi'_j(\boldsymbol{x}')) = E_0\nabla'\cdot(\boldsymbol{\tau}'(\boldsymbol{x}')\cdot\hat{\boldsymbol{e}}_j) \\ \Phi'_j(\boldsymbol{x}') \to 0 \qquad \text{as} \quad |\boldsymbol{x}'|\to\infty \end{cases} \qquad \boldsymbol{x}'\in\mathbb{R}^3$$

or in the unscaled coordinates

$$\begin{cases} \alpha^{-2}\nabla\cdot((\boldsymbol{\tau}(\boldsymbol{x})+\mathbf{I})\cdot\nabla\Phi'_j(\alpha\boldsymbol{x})) = E_0\alpha^{-1}\nabla\cdot(\boldsymbol{\tau}(\boldsymbol{x})\cdot\hat{\boldsymbol{e}}_j) \\ \Phi'_j(\alpha\boldsymbol{x}) \to 0 \qquad \text{as} \quad |\boldsymbol{x}|\to\infty \end{cases} \qquad \boldsymbol{x}\in\mathbb{R}^3.$$

Due to the unique solubility of the boundary value problem (A.2), $\Phi'_j(\boldsymbol{x}') = \alpha\Phi_j(\boldsymbol{x})$, and consequently $\boldsymbol{E}'_j(\boldsymbol{x}') = \boldsymbol{E}_j(\boldsymbol{x}) = \boldsymbol{E}_j(\boldsymbol{x}'/\alpha)$. The polarizability dyadic for the scaled problem then becomes

$$\hat{\boldsymbol{e}}_i\cdot\boldsymbol{\gamma}'\cdot\hat{\boldsymbol{e}}_j = \hat{\boldsymbol{e}}_i\cdot\int_{\mathbb{R}^3}\boldsymbol{\tau}'(\boldsymbol{x}')\cdot\boldsymbol{E}'_j(\boldsymbol{x}')\,\mathrm{dV}_{\boldsymbol{x}'} = \alpha^3\hat{\boldsymbol{e}}_i\cdot\int_{\mathbb{R}^3}\boldsymbol{\tau}(\boldsymbol{x})\cdot\boldsymbol{E}_j(\boldsymbol{x})\,\mathrm{dV}_{\boldsymbol{x}},$$

and we see that $\boldsymbol{\gamma}$ scales with the volume $|V|\sim\alpha^3$.

A.1. Symmetry

The polarizability dyadic $\boldsymbol{\gamma}$ is symmetric, since $\boldsymbol{\tau}$ is assumed symmetric at all points $\boldsymbol{x}$. In fact, from (A.3),

$$\hat{\boldsymbol{e}}_i\cdot\boldsymbol{\gamma}\cdot\hat{\boldsymbol{e}}_j = \hat{\boldsymbol{e}}_i\cdot\int_{\mathbb{R}^3}\boldsymbol{\tau}(\boldsymbol{x})\cdot\hat{\boldsymbol{e}}_j\,\mathrm{dV}_{\boldsymbol{x}} - \frac{1}{E_0}\hat{\boldsymbol{e}}_i\cdot\int_{\mathbb{R}^3}\boldsymbol{\tau}(\boldsymbol{x})\cdot\nabla\Phi_j(\boldsymbol{x})\,\mathrm{dV}_{\boldsymbol{x}}. \tag{A.4}$$

The last integral in (A.4) is rewritten as

$$\begin{aligned} \hat{\boldsymbol{e}}_i\cdot\int_{\mathbb{R}^3}\boldsymbol{\tau}(\boldsymbol{x})\cdot\nabla\Phi_j(\boldsymbol{x})\,\mathrm{dV}_{\boldsymbol{x}} &= \int_{\mathbb{R}^3}\nabla\cdot(\hat{\boldsymbol{e}}_i\cdot\boldsymbol{\tau}(\boldsymbol{x})\Phi_j(\boldsymbol{x}))\mathrm{dV}_{\boldsymbol{x}} - \int_{\mathbb{R}^3}\nabla\cdot(\hat{\boldsymbol{e}}_i\cdot\boldsymbol{\tau}(\boldsymbol{x}))\,\Phi_j(\boldsymbol{x})\,\mathrm{dV}_{\boldsymbol{x}} \\ &= -\int_{\mathbb{R}^3}\nabla\cdot(\boldsymbol{\tau}(\boldsymbol{x})\cdot\hat{\boldsymbol{e}}_i)\,\Phi_j(\boldsymbol{x})\,\mathrm{dV}_{\boldsymbol{x}} \\ &= -\frac{1}{E_0}\int_{\mathbb{R}^3}\nabla\cdot((\boldsymbol{\tau}(\boldsymbol{x})+\mathbf{I})\cdot\nabla\Phi_i(\boldsymbol{x}))\,\Phi_j(\boldsymbol{x})\,\mathrm{dV}_{\boldsymbol{x}}, \end{aligned}$$

due to (A.2) provided $\boldsymbol{\tau}$ is symmetric at all points $\boldsymbol{x}$. Furthermore,

$$\begin{aligned} \hat{\boldsymbol{e}}_i\cdot\int_{\mathbb{R}^3}\boldsymbol{\tau}(\boldsymbol{x})\cdot\nabla\Phi_j(\boldsymbol{x})\,\mathrm{dV}_{\boldsymbol{x}} &= -\frac{1}{E_0}\int_{\mathbb{R}^3}\nabla\cdot\{((\boldsymbol{\tau}(\boldsymbol{x})+\mathbf{I})\cdot\nabla\Phi_i(\boldsymbol{x}))\Phi_j(\boldsymbol{x})\}\,\mathrm{dV}_{\boldsymbol{x}} \\ &\quad + \frac{1}{E_0}\int_{\mathbb{R}^3}\nabla\Phi_j(\boldsymbol{x})\cdot((\boldsymbol{\tau}(\boldsymbol{x})+\mathbf{I})\cdot\nabla\Phi_i(\boldsymbol{x}))\,\mathrm{dV}_{\boldsymbol{x}} \\ &= \frac{1}{E_0}\int_{\mathbb{R}^3}\nabla\Phi_j(\boldsymbol{x})\cdot((\boldsymbol{\tau}(\boldsymbol{x})+\mathbf{I})\cdot\nabla\Phi_i(\boldsymbol{x}))\,\mathrm{dV}_{\boldsymbol{x}}. \end{aligned}$$

The polarizability dyadic (A.4) therefore becomes

$$\hat{\boldsymbol{e}}_i \cdot \boldsymbol{\gamma} \cdot \hat{\boldsymbol{e}}_j = \hat{\boldsymbol{e}}_i \cdot \int_{\mathbb{R}^3} \boldsymbol{\tau}(\boldsymbol{x}) \cdot \hat{\boldsymbol{e}}_j \, \mathrm{dV}_{\boldsymbol{x}} - \frac{1}{E_0^2} \int_{\mathbb{R}^3} \nabla \Phi_j(\boldsymbol{x}) \cdot ((\boldsymbol{\tau}(\boldsymbol{x}) + \mathbf{I}) \cdot \nabla \Phi_i(\boldsymbol{x})) \, \mathrm{dV}_{\boldsymbol{x}},$$

which clearly is symmetric in the indices i and j if $\boldsymbol{\tau}$ is symmetric at all points $\boldsymbol{x}$.

A.2. High-contrast limit

In the high-contrast limit, when the entries of the material dyadic become infinitely large independent of $\boldsymbol{x}$, the appropriate surface integral representation of the polarizability dyadic is [15, p 22]

$$\hat{\boldsymbol{e}}_i \cdot \boldsymbol{\gamma} \cdot \hat{\boldsymbol{e}}_j = \frac{1}{E_0} \hat{\boldsymbol{e}}_i \cdot \sum_{n=1}^{N} \int_{S_n} (\hat{\boldsymbol{\nu}}(\boldsymbol{x}) \Phi_j(\boldsymbol{x}) - \boldsymbol{x} \hat{\boldsymbol{\nu}}(\boldsymbol{x}) \cdot \nabla \Phi_j(\boldsymbol{x})) \, \mathrm{dS}_{\boldsymbol{x}},$$

where $S_n, n = 1, 2, \ldots, N$, denote the bounding surfaces (outward-directed unit normal $\hat{\boldsymbol{\nu}}$) of the domain outside the material (we assume that $\boldsymbol{\tau}$ is compactly supported). Moreover, $\Psi_j(\boldsymbol{x}) = \Phi_j(\boldsymbol{x}) - E_0 x_j$ is the solution to ($n = 1, 2, \ldots, N$)

$$\begin{cases} \nabla^2 \Psi_j(\boldsymbol{x}) = 0, & \boldsymbol{x} \text{ outside } S_n \\ \displaystyle\int_{S_n} \hat{\boldsymbol{\nu}}(\boldsymbol{x}) \cdot \nabla \Psi_j(\boldsymbol{x})|_+ \, \mathrm{dS}_{\boldsymbol{x}} = 0 \\ \Psi_j(\boldsymbol{x}) \to -E_0 x_j + \mathcal{O}(|\boldsymbol{x}|^{-2}) \qquad \text{as} \quad |\boldsymbol{x}| \to \infty. \end{cases}$$

With similar arguments as above, we find that the eigenvalues of the high-contrast polarizability dyadic also scale with the volume. For the relation with the capacitance concept, we refer to [15].

References

[1] Abramowitz M and Stegun I A (ed) 1970 *Handbook of Mathematical Functions (Applied Mathematics Series* vol 55*)* (Washington, DC: National Bureau of Standards)

[2] Beard K V and Chuang C C 1986 A new model for the equilibrium shape of raindrops *J. Atmos. Sci.* **44** 1509–24

[3] Björkberg J and Kristensson G 1987 Electromagnetic scattering by a perfectly conducting elliptic disk *Can. J. Phys.* **65** 723–34

[4] Bohren C F and Huffman D R 1983 *Absorption and Scattering of Light by Small Particles* (New York: Wiley)

[5] Chu L J 1948 Physical limitations of omni-directional antennas *Appl. Phys.* **19** 1163–75

[6] Collin R E 1991 *Field Theory of Guided Waves* 2nd edn (New York: IEEE)

[7] Gustafsson M, Sohl C and Kristensson G Physical limitations on antennas of arbitrary shape *Proc. R. Soc.* A **463** 2007

[8] Gustafsson M 2003 On the non-uniqueness of the electromagnetic instantaneous response *J. Phys. A: Math. Gen.* **36** 1743–58

[9] John F 1948 Extremum problems with inequalities as subsidiary conditions *Studies and Essays: Courant Anniversary Volume* ed O E Friedrichs, K O Neugebauer and J J Stoker (New York: Wiley-Interscience) pp 187–204

[10] Jones D S 1979 Low frequency electromagnetic radiation *J. Inst. Math. Appl.* **23** 421–47

[11] Jones D S 1985 Scattering by inhomogeneous dielectric particles *Quart. J. Mech. Appl. Math.* **38** 135–55

[12] Jones R C 1945 A generalization of the dielectric ellipsoid problem *Phys. Rev.* **68** 93–6

[13] Jung H W E 1901 Über die kleinste Kugel, die eine räumliche Figur einschliesst *J. Angew. Math.* **123** 241–57

[14] Kaatze U 1996 Microwave dielectric properties of water *Microwave Aquametry* ed A Kraszewski (New York: IEEE) chapter 2, pp 37–53

[15] Kleinman R E and Senior T B A 1986 Rayleigh scattering *Low and High Frequency Asymptotics (Acoustic, Electromagnetic and Elastic Wave Scattering* vol 2*)* ed V V Varadan and V K Varadan (Amsterdam: Elsevier) chapter 1, pp 1–70

[16] Landau L D, Lifshitz E M and Pitaevskiĭ L P 1984 *Electrodynamics of Continuous Media* 2nd edn (Oxford: Pergamon)
[17] Mie G 1908 Beiträge zur Optik trüber Medien, speziell kolloidaler Metallösungen *Ann. Phys., Lpz.* **25** 377–445
[18] Mishchenko M I and Travis L D 1998 Capabilities and limitations of a current FORTRAN implementation of the *T*-matrix method for randomly oriented, rotationally symmetric scatterers *J. Quantum Spectrosc. Radiat. Transfer* **60** 309–24
[19] Newton R G 2002 *Scattering Theory of Waves and Particles* 2nd edn (New York: Dover)
[20] Nussenzveig H M 1972 *Causality and Dispersion Relations* (London: Academic)
[21] Nussenzveig H M 1992 *Diffraction Effects in Semiclassical Scattering* (Cambridge: Cambridge University Press)
[22] Osborn J A 1945 Demagnetizing factors of the general ellipsoid *Phys. Rev.* **67** 351–7
[23] Purcell E M 1969 On the absorption and emission of light by interstellar grains *J. Astrophys.* **158** 433–40
[24] Sihvola A, Ylä-Oijala P, Järvenpää S and Avelin J 2004 Polarizabilities of Platonic solids *IEEE Trans. Antennas Propagat.* **52** 2226–33
[25] Sohl C, Gustafsson M and Kristensson G 2007 Physical limitations on metamaterials: restrictions on scattering and absorption over a frequency interval *Technical Report* LUTEDX/(TEAT-7154)/1–10/(2007) (Lund, Sweden: Department of Electrical and Information Technology, Lund University) http://www.eit.lth.se
[26] Strutt J W 1871 On the light from the sky, its polarization and colour *Phil. Mag.* **41** 107–20 and 274–9 (Also published in Rayleigh L 1899 *Scientific Papers* vol I) (Cambridge: Cambridge University Press)
[27] Taylor J R 1983 *Scattering Theory: The Quantum Theory of Nonrelativistic Collisions* (Malabar, FL: Krieger)
[28] Titchmarsh E C 1948 *Introduction to the Theory of Fourier Integrals* 2nd edn (Oxford: Oxford University Press)
[29] van de Hulst H 1957 *Light Scattering by Small Particles* (New York: Wiley)
[30] Yaghjian A D 1980 Electric dyadic Green's functions in the source region *Proc. IEEE* **68** 248–63